Advancements on the use of Filtered Rayleigh Scattering (FRS) with Machine learning methods for flow distortion in Aero-Engine intakes

Matteo Migliorini [a],[*], Ulrich Doll [b], Nicholas J. Lawson [c], Sergey M. Melnikov [d], Jonas Steinbock [d], Michael Dues [d], Pavlos K. Zachos [a], Ingo Röhle [e], David G. MacManus [a]

[a] Centre for Propulsion and Thermal Power Engineering, Cranfield University, Bedfordshire MK43 0AL, UK
[b] Department of Mechanical and Production Engineering, Aarhus University, Katrinebjergvej 89, Aarhus 8200, Denmark
[c] Aerospace Engineering, University of Sydney, Camperdown, NSW 2006, Australia
[d] ILA R&D GmbH, Rudolf-Schulten-Straße 3, Jülich 52428, Germany
[e] Berliner Hochschule für Technik, Luxemburger Str. 10, Berlin 13353, Germany

ARTICLE INFO

ABSTRACT

In-flight measurements of aerodynamic quantities are a requirement to ensure the correct scaling of Reynolds and Mach number and for the airworthiness certification of an aircraft. The ability to obtain such measurement is subject to several challenges such as instrument installation, environment, type of measurand, and spatial and temporal resolution. Given expected, more frequent use of embedded propulsion systems in the near future, the measurement technology needs to adapt for the characterization of multi-type flow distortion in complex flow, to assess the operability of air-breathing propulsion systems. To meet this increasing demand for high-fidelity experimental data, the Filtered Rayleigh Scattering (FRS) method is identified as a promising technology, as it can provide measurements of pressure, temperature and 3D velocities simultaneously, across a full Aerodynamic Interface Plane (AIP). This work demonstrates the application of a novel FRS instrument, to assess the flow distortion in an S-duct diffuser, in a ground testing facility. A comparison of FRS results with Stereo-Particle Image Velocimetry (S-PIV) measurements reveals good agreement of the out of plane velocities, within 3.3 % at the AIP. Furthermore, the introduction of machine learning methods significantly accelerates the processing of the FRS data by up to 200 times, offering a substantial prospect towards real time data analysis. This study demonstrates the further development of the FRS technique, with the ultimate goal of inlet flow distortion measurements for in-flight environments.

1. Introduction

International aviation strategic reports from EASA, NASA, and ICAO call for a dramatic reduction in CO2 and NOx emissions [1–3]. Achieving the specified sustainability targets is expected to heavily rely on the development of a green hydrogen infrastructure and sustainable aviation fuel for the de-carbonization [4], but crucially also on the development of more efficient, novel propulsion systems, closely-integrated with the airframe to achieve further benefits in installed system efficiency [5]. This may lead to unconventional architectures like boundary layer ingestion (BLI) and distributed propulsion systems, requiring substantial developments to both the airframe and propulsion system. However, the potential benefits of these novel configurations can be penalized by the increased level of distortion, that closely

coupled propulsion systems may face, by the compact and potentially convoluted intake configurations [6,7]. Recent experiments demonstrated that embedded engine configurations are subjected to dynamic total pressure and swirl distortion at the propulsor inlets during the aircraft mission, and that the flow structures at the engine inlet are much more complex, compared to traditional podded engines [8]. This is of key importance to aircraft certification, whereby the engine must demonstrate safe operation throughout the full operative envelop, which includes ground operation, taxiing, take-off, cruise and landing [9].

In aircraft aerodynamics, flow scaling is dominated by the two dimensionless quantities Reynolds number (Re) and Mach number (*M*). In environments where compressibility is a consideration, wind tunnels are generally not be able to simultaneously match Re and *M*. Only two facilities in the world, the NASA National Transonic Facility (NTF) and

Nomenclature

A	Area, m^2	PIV	Particle Image Velocimetry
AIP	Aerodynamic Interface Plane	r	Radial coordinate, m
D_{in}	S-duct inlet plane diameter, mm	R	Radius, m
D_{out}	S-duct outlet plane diameter, mm	RBS	Rayleigh-Brillouin Scattering
DGV	Doppler Global Velocimetry	Re	Reynolds number
FRS	Filtered Rayleigh Scattering	RMSE	Root mean square error
H	S-duct vertical offset, m	SAE	Society of Automotive Engineers
L	S-duct length, m	SNR	Signal-to-Noise Ratio
M	Mach number	T_{ref}	Reference ambient temperature, K
ML	Machine Learning	T_s	Static temperature, K
MLFRS	Machine Learning model for the Filtered Rayleigh Scattering spectra	V	Velocity component, m/s
		X	Horizontal coordinate
MLRBS	Machine Learning model for the Rayleigh-Brillouin Scattering	Y	Vertical coordinate
		Z	Streamwise coordinate
		α	Azimuthal angle of camera view, °
P_{ref}	Reference ambient pressure, Pa	β	Polar angle of camera view, °
P_s	Static pressure, Pa	λ	Wavelength, nm

the DLR European Transonic Wind Tunnel (DLR) can achieve this. However, access to these facilities is very limited, due to demand and high running costs. As a result, in-flight measurements must be considered as a route to obtain representative results. However, traditional measurement methods for in-flight applications present notable challenges linked to the installation of the instrument, the environment in which the instruments must operate, or the measurand that can be recorded [10]. Nevertheless, engine manufacturers have acknowledged that in-flight tests with instrumented engines are crucial to cover the full range of operating conditions that the engine can experience [11,12]. Indeed, the flight envelope consists of conditions which are difficult to reproduce during ground tests. At the same time, however, a key requirement is also to develop instrumentation which can resolve the flow distortion characteristics through measurements with high resolution in space and time. In the published literature there are limited examples of instrumentation that has been successfully developed for in-flight measurements, for example unsteady total pressure rakes [13]. However, arguably, these cannot adequately to capture the spatial complexity of the distorted flow field expected in novel aircraft configurations [8], due to the low number of measurement points across the plane. Similarly, they also show poor ability to characterize other types of flow distortion such as swirl and temperature. Increasing the number or variety of intrusive instrumentation may not be feasible because of the induced blockage and also due to the certification requirements that in-flight measurement systems have to adhere to [13].

Laser-based optical methods, such as particle image velocimetry (PIV), have recently overcome some of these limitations of traditional methods [14,15]. These optical methods are typically non-intrusive and offer high spatial resolution and high sampling rates [16]. For example, Particle Image Velocimetry (PIV) [17] and Doppler Global Velocimetry (DGV) [18] are planar laser-based optical techniques that can capture time-averaged and unsteady swirl distortion. Stereo PIV has been used for swirl measurements in civil intake configurations [19], and also in convoluted S-duct diffusers [20]. These unsteady PIV measurements unlocked the understanding of fundamental flow structures [21,22] and the effect of inlet conditions on to the inherent flow distortion for subsonic diffusers [23,24]. DGV was implemented in an aircraft model to characterize the time-averaged swirl distortion inside the intake duct for an embedded propulsion system [25]. Miniature light sheet optics and optical wave guides were used to overcome the challenges of optical access and measurement system integration inside confined flow systems. Nevertheless, both DGV and PIV techniques require the use of tracer particles, which has several drawbacks, including the uncertainties in the seeding distribution and density, the need of seeding

rakes and the errors induced by the optical distortion. In particular, this poses great challenges for the implementation of these techniques in an airborne setting [26].

In response to pertinent shortcomings of laser-optical methods relying on tracer particles, the seeding-free Filtered Rayleigh Scattering (FRS) technique has recently been reviewed in the context of characterizing aerospace engine inlet flow distortions for both ground and flight testing [26–28]. It has been concluded that the technique has an immediate high development potential for inlet flow distortion testing. This stems from the fact that no tracer particles are required to seed the flow, the low optical access requirements due to optical probe technology and the method's unique ability to simultaneously measure two dimensional static pressure, temperature and three-component (3C) velocity fields [29]. Previous multi-property measurements by FRS, however, have been limited to obtaining time-averaged results and current research aims at enabling time-resolved measurements. In this context, a variant of an FRS system which exploits multiple perspective views has been developed [30] and recently verified on a simple ducted flow experiment [31]. It is the aim of this work to further mature this FRS implementation towards multi-property flow measurements in a complex ground testing facility and, ultimately, in-flight measurements.

Within this context, the aim of this paper is to present high-resolution, non-intrusive flow characterizations using FRS. This work will lead to a roadmap with real-time measurements and in-flight implementation of the method. The work also demonstrates the future capability of FRS measurements, giving solutions for optical access and camera integration, in which are required for in-flight implementation. Further, the use of machine learning methods to enable and real-time flow diagnostics are also discussed.

2. Experimental setup and methods

2.1. Cranfield complex intake test facility

In an effort to increase the Technology Readiness Level (TRL) of the FRS laser diagnostic instrument demonstrated in a concept system design [30], the technology has been implemented in the Cranfield Complex Intakes Test Facility (CCITF) (Fig. 1). This represents a fundamental step in demonstrating the measurement system capability for air induction systems, ahead of the future application for ground and in-flight testing. A bell mouth opening is used to draw air into the rig and honeycomb mesh panels are used to uniform the flow (Fig. 1). Downstream of the straighteners, the cross-sectional area of the rig reduces through a convergent nozzle to match the inlet diameter of the selected
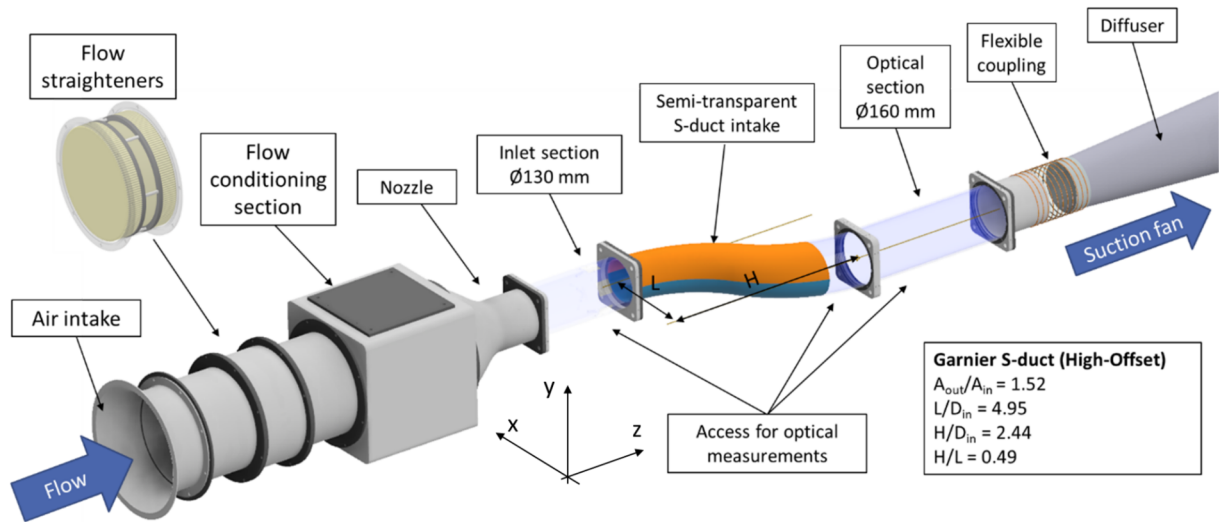
Fig. 1. 3D rendering of the Cranfield Complex Intake Test Facility (CCITF).

S-duct diffuser. The convergent also helps in further improving the flow quality [32]. The diffuser has been widely investigated previously. Key geometrical specifications are reported in Fig. 1. Total pressure and swirl distortion, impact of non-uniform inlet conditions, influence of Mach number, and the use of flow control methods have been published in the peer-reviewed literature [20,21,33–37]. The measurement plane was located at the exit of the S-duct diffuser, where a cylindrical section with anti-reflective coating offers optical access for the non-intrusive measurement. The prime mover of the rig was a centrifugal fan which is located downstream with a flexible coupling and flow diffuser (Fig. 1). Additional experimental details are included in previous work by Migliorini et. al. [38].

The operating point was defined at the inlet centreline Mach number M_{ref} measured 1.0 D_{in} upstream of the S-duct diffuser inlet plane. The operating Mach number targeted for the experimental work was between 0.18–0.40. Tests conducted at $M_{ref} = 0.27$ are reported in this manuscript as this operating point is common among multiple publications in the peer-reviewed literature [20,21,33–37]. The inlet Mach number M_{ref} was defined as a function of the wall static pressure ($P_{S,in}$) measured through 8 circumferentially equi-spaced and pneumatically averaged static ports which were located 3.17 D_{in} upstream the S-duct diffuser inlet plane and the ambient pressure ($P_{ref,amb}$). A calibration process determined the correlation between inlet Mach number (M_{ref}) and the ratio between the wall static pressure ($P_{S,in}$) and the ambient pressure ($P_{ref,amb}$). Based on the correlation, the wall static pressure ($P_{S,in}$) and the ambient pressure ($P_{ref,amb}$) are monitored to enable the real time calculation of the inlet Mach number M_{ref} and the system is controlled with a feedback loop. The uncertainty on the operating Mach number has been evaluated, taking into consideration the propagation of the uncertainty of the measured wall static pressure ($P_{S,in}$), the ambient pressure (P_{amb}), and the regression errors of the inlet Mach number (M_{ref}) formulation. Overall, the combined uncertainty on Mach number for the conditions used in this work was $M_{ref} = 0.27 \pm 0.006$.

2.2. Filtered Rayleigh Scattering measurements

The seeding-free FRS method relies on the spectral discrimination between elastic laser light scattering from gas molecules, which holds information on density, pressure, temperature and flow velocity, and unwanted laser stray light from surfaces or large particles (Mie scattering) by means of molecular absorption [39]. The combined measurement of multiple flow properties by FRS is typically achieved by applying a frequency scanning technique [40–42]. By combining this

method with at least three camera perspectives to reconstruct the three velocity components from the measured optical Doppler frequency shifts, the simultaneous measurement of static pressure, temperature and 3C velocity fields was achieved [29]. Since frequency scanning is time consuming, multi-parameter FRS measurements have so far only been time averaged. By extending the multiple view imaging approach to at least five perspectives and thus matching the number of unknown flow variables (pressure, temperature and three velocity components), their combined measurement based on a single excitation frequency becomes feasible, opening the path towards unsteady multi-property flow diagnostics by FRS [26]. Based on this general idea, a six-view observation concept was developed [30] and recently verified on a simple ducted flow [31]. As will be briefly discussed in more detail below, a relative movement of the CCITF test section to the installed detection setup made a single frequency measurement unfeasible and therefore frequency scanning had to be used. Although, strictly speaking, only three perspectives would be required, the observation concept with six views offers distinct advantages in terms of reducing measurement uncertainty and coverage of the plane of interest. Further information on the background treatment and selected number of views can be found in [38].

An overview of the FRS system components is provided in Fig. 2a. The instrument leverages a 532 nm continuous-wave (CW) fibre laser from Azur-Light as its light source. This laser offers a variable output power from 0.1 to 6 W and in this work it operated at 5 W. A spectral linewidth below 200 kHz is achieved through an external NKT Photonics ADJUSTIK Y10 seed laser unit. The laser features both fast piezo and thermal tuning mechanisms, enabling precise adjustments of its output frequency; piezo tuning offers a fine-grained 10 GHz range, while thermal tuning grants access to a broader 700 GHz emission spectrum. The laser frequency is actively controlled by sampling a portion of laser light into a HighFinesse WS8 wavelength-meter (wlm), resulting in a deviation of below 1 MHz to the set value. To account for thermal drifts, the device is regularly calibrated with a frequency-stabilised Helium-Neon (He-Ne) laser. A second branch is used to continuously monitor the laser's output power with a power metre (pm). The main laser beam is guided through an articulated mirror arm (ama) into a light sheet generator (lsg) that expands the laser beam to a height of approximately 100 mm using an optical scanner arrangement. The polarization of the laser beam is aligned with the laser sheet plane with a half-wave plate ($\lambda/2$). As indicated in Fig. 2c the laser sheet is oriented at an angle of 45° to the measuring plane to obtain symmetrically distributed uncertainties, of the in-plane velocity components. Since the size of the laser sheet is only sufficient to illuminate half of the channel cross
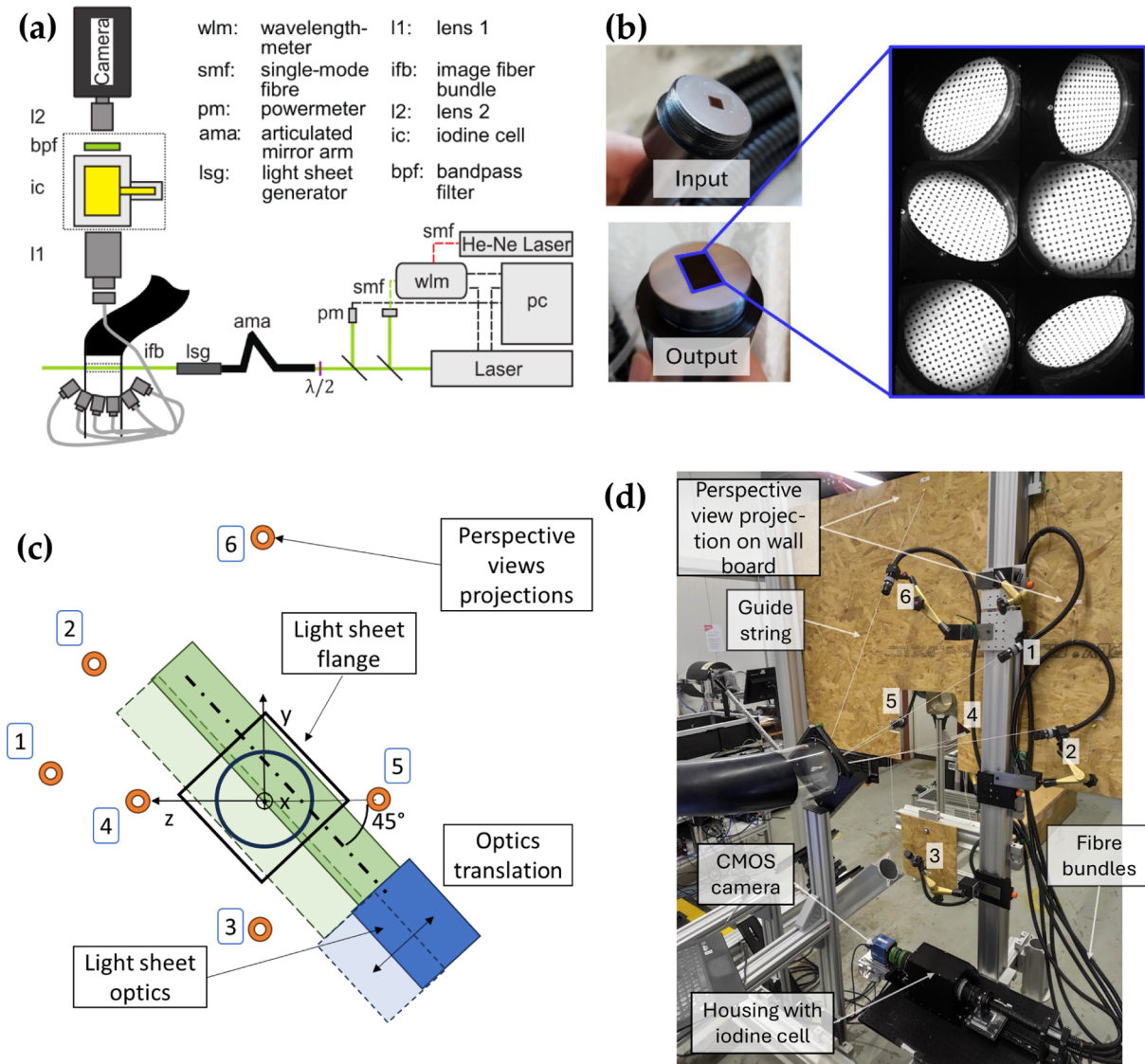
Fig. 2. (a) Overview of FRS system components (adapted from [31]). (b) Input and output sides of the image fibre bundle with a snapshot of a calibration target mounted at the measurement plane showing the six perspectives. (c) Optical arrangement of the FRS fibre bundle cameras and laser light sheet at the AIP of the S-duct intake. (d) Photograph of the camera alignment procedure.

section, measurements are repeated after shifting it to the other half, to obtain two corresponding data sets. Nevertheless, it is envisaged that by adapting the light sheet optics and using a higher power laser system, it would be possible to carry out the same measurements in a single acquisition. The FRS system is aligned to capture data at 0.2 D_{in} downstream of the S-duct outlet plane. For further information on the laser sheet optics and the adaption to the test facility, refer to Migliorini et al. [38].

The optical imaging system employs a six-branch image fibre bundle (ifb, Fig. 2a) to capture multiple perspectives within a single light-sensitive area at its distal end. Each branch has a length of 2.5 m and acts as a dedicated channel for a distinct view, effectively eliminating the need for multiple physical cameras and iodine filter cells (Fig. 2b). Additionally, the flexible fibre bundles can be installed like normal electrical cables and light collection can occur with minimal optical accessibility through optical probes, making the technology a key asset for future in-flight FRS implementations. In this work, light scattered from the measurement plane enters each branch through its corresponding input lens (1.4f-number, 16 mm focal length). The signal is focused on a light sensitive area of 16 mm^2, which contains a total of 400 x 400 fibres with 10 μm core diameter, having a manufacturer

specified transmission of 40 %, Fig. 2b input. At the distal end, the different perspectives converge into a single rectangular area of 12 x 8 mm^2 (Fig. 2b output) subdivided into regions that correspond to the individual perspectives. Following image collection with the ifb, the light passes through the transfer optics (l1, l2) with a molecular iodine filter cell (ic) and a bandpass filter (bpf, 10 nm FWHM @ 532 nm) in between, and is finally focused on the camera sensor (CMOS, PCO Edge 4.2). The full system including lenses, fibre bundles, iodine cell and camera is shown in Fig. 2d. An example of the final image of the calibration plate from the 6 perspective views is included in Fig. 2b.

To minimise uncertainties in the measured variables, the fibre bundle front ends are positioned as close as possible to the optimised configuration presented in Doll et. al [30]. As indicated in Fig. 2 (c), the input sides are oriented on a virtual sphere downstream from the AIP. To align the optimised perspectives at the test facility, the camera positions are back projected on a wooden board located at a specified downstream distance, Fig. 2 (d). Tensioned guide strings act as alignment aid by installing them from the AIP centre to the projected camera position on the wooden board. The fibre bundles are then positioned along these strings at a prescribed radial distance and secured with hydraulic magnetic measuring stands. Following the alignment procedure, the

individual camera perspectives are calibrated using Python's OpenCV toolbox [43]. Due to physical restrictions imposed by the test facility's support structure, the installed camera configuration slightly deviates from the optimal positioning. The six optimised camera positions, indicated by the azimuthal (α) and polar angles (β) [30], as well as the installed perspectives in spherical coordinates, are compared in Table 1. Even though the differences for some perspectives are noteworthy, the impairment of accuracy for the frequency scanning measurements is expected to be small.

In the further data processing, the images were divided into six individual images, each of which corresponds to a specific perspective. After extracting the control point locations from the calibration image, this information is used to rectify the images and map them onto a common Cartesian grid. This procedure results in a spatial resolution of 1 pixel/mm. Depending on the perspective, optical accessibility to the AIP is partly obstructed by the light sheet flange. The resulting overlap between the different views is visualised in Fig. 3. The minimum number of three perspectives have coverage of almost the entire channel cross section. However, during processing it was found that the results for only three or four perspectives are less reliable [38]. Therefore, it was decided to only consider regions with a minimum of five usable views, which excludes a larger portion of the AIP on the upper left but, nevertheless, covers about 88 % of the total area.

A full FRS dataset consists of reference data measured under controlled conditions with no flow and known temperature and pressure, and the flow data that is measured under actual flow conditions. Both reference and flow data involve frequency scanning the laser output for 37 distinct frequencies within the blocking region of the iodine filter, and an image is acquired at each frequency step; the exposure time for each image is 20 s. To further increase the signal-to-noise-ratio (SNR), each measurement is repeated five times, and the results are averaged. In this procedure, the reference frequency scan is used to derive a calibration constant and a background parameter for each resolution element and perspective. Under the assumption that these parameters do not change, the flow data is then analyzed to retrieve the desired flow variables. However, since the relative movement between the FRS instrument and the test section cause these experimental parameters to change from reference to flow conditions, the standard methodology cannot be applied. Instead, a normalization procedure has to be used [44], and background parameters have to be included in the fitting procedure. Please refer to [38] for more details on the implementation.

2.3. Machine learning methods for rapid processing of FRS data

The availability of real-time inlet flow distortion conditions during a flight mission would enable the propulsion system to respond to the changing operating conditions to tolerate the flow distortion and maintain reliability during operation. This data could be fed to the control system for rapid adaptation, for example by adopting counter-measures to prevent surge and loss of power. However, this is subject to real-time processing capability. For evaluating FRS data, the numerical description of the Rayleigh-Brillouin Scattering (RBS) spectrum is a computationally demanding task [45]. This becomes a significant issue
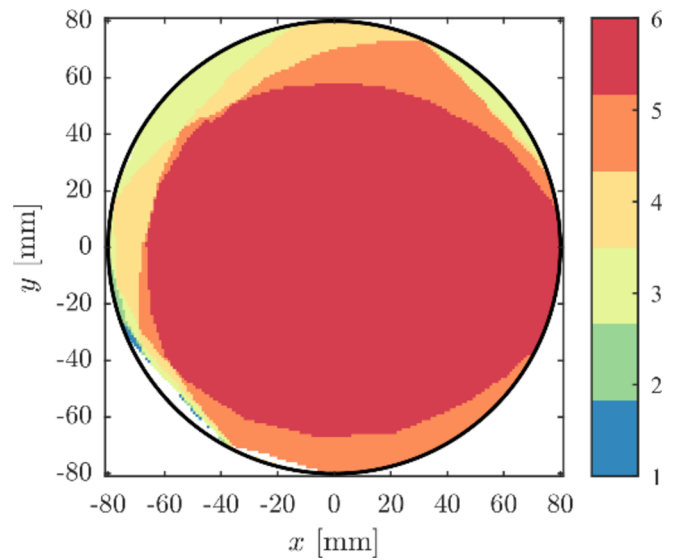

Fig. 3. Coverage of the measurement plane showing the number of overlapping views at each region of the measurement plane.

especially in the case presented, where the characterization of the AIP flow conditions requires space-resolved FRS measurements across the full plane. Existing fast analytical approximations [44,46–48] of well-established physics-based models, such as the Tenti S6 [49] and the Pan S7 [50], are not stable enough or not equally applicable in wider gas flow regimes. This opens the route to the use of robust machine learning (ML) methods to accelerate the computations towards real-time FRS evaluations.

Machine learning has already been used to carry out fast approximation of the RBS profiles [31,45]. The core functions of the ML algorithms are support vector regression methods, which are a set of supervised learning methods adapted from the scikit-learn software package [51]. These approximate measurement or simulated data, based on numerical regularities, and without any knowledge of the underlying physics. Such computational algorithms can provide acceleration of data processing, as they bypass the need to solve complicated equations for the prediction. A teaching procedure is required to create ML predictive functions with preparative computations. The training set which consists of numerical regularities is used to relate the input model parameter sets with the output profiles. In this application, this is a set of RBS profiles, corresponding to all parameter variations expected in forthcoming measurements. These curves can be either generated numerically, with one of the established models, or obtained directly from an experiment. All preparative calculations, including the generation of the training set and the teaching procedure, are carried out in regular desktop machines within minutes. A notable benefit of the ML approach is its ability to quickly rebuild the prediction function for a different input parameter set, or parameter range.

Two ML-models for FRS data processing have been generated. The first one (MLRBS) generates fast predictions of the RBS profile. The MLRBS model is based on the calibrated analytical RBS representation published in [44] and was used in the data analysis throughout this manuscript. Application of this model for the data evaluation provided a 20-fold decrease of computational time, in comparison to the conventional methods using the Tenti model. Additionally, a second, novel approach (MLFRS) is introduced that directly approximates the measured FRS intensity spectra. This removes the necessity of calculating the convolution between RBS spectrum and iodine filter transmission curve, which is another computational intensive and, thus, time-consuming operation. Details of the applied algorithms, tuning parameters and software implementations can be found in [52]. The MLFRS produces a 200-fold decrease in processing time compared to the

Table 1
Spherical coordinates of the optimised and installed camera positions.

	Optimised		Installed		
	$\alpha[°]$	$\beta[°]$	$\alpha[°]$	$\beta[°]$	$R[mm]$
View 1	50.0	141.0	49.5	140.3	655.0
View 2	47.7	172.0	47.0	172.5	695.5
View 3	48.8	270.0	47.6	261.8	625.2
View 4	16.0	175.5	12.2	201.8	649.7
View 5	25.9	350.9	11.2	1.3	662.3
View 6	50.0	90.0	57.6	89.5	643.7

conventional processing,without ML methods, when tested on the same computer. Thus, the use of this method may offer a route for real-time FRS data processing, which is relevant for an in-flight application.

2.4. S-PIV

Stereo Particle Image Velocimetry was used to benchmark the FRS measurement system. The full system has been published by Zachos et. al [20] and only a short summary is reported hereby for brevity. A pair of CMOS cameras with a pixel resolution of 1280 x 800 was used to image through the optical walls of the S-duct diffuser and measure the 3D velocity components at the S-duct outlet plane (0.0 D_{out}). DEHS seeding particles with 1 μm average diameter were illuminated by a pulsed Nd: YAG laser, at a cross-flow plane. In each plane, 20,000 velocity flow-fields were acquired at a frequency of 8 kHz and then time-averaged for the comparative assessment with the FRS measurements. The final spatial resolution of the PIV measurements was 2.3 x 2.3 mm^2 (0.0144 D_{AIP}) and the total number of 3D velocity vectors across the plane was approximately 3,000. A disparity correction reduced the errors induced by the inevitable alignment errors between calibration plate and laser light, to sub-pixel scale. Only the data within $r/R_{AIP} < 0.9$ was considered for the analysis, to remove the spurious velocity vectors, caused by laser light reflections in the optical domain. The data processing has been carried out with *LaVision Davis* software version 10.2.1. The uncertainty of the velocity components is 3.3 % of the area-averaged, time-averaged streamwise velocity, at the AIP based on the method of Raffel et. al [17]. Due to the higher spatial resolution of FRS measurements compared with PIV, the FRS data has been interpolated with a cubic fit on the PIV grid resolution. The RSME has been obtained with the comparison of the data along X = 0 and Y = 0 at the S-duct outlet plane, exclusively for areas in which both measurements were available.

3. Results and discussion

3.1. Full-plane 3-component velocity measurements in complex intakes

The aerodynamics of S-duct diffusers is predominantly influenced by the presence of secondary flows and flow separations. Because of its high momentum, the core flow is relatively less affected by the S-duct turning and tends to displace towards the outside of the bend, due to the adverse pressure gradient [53]. On the other hand, the effect of the turning is greater in the low momentum boundary layer region, which tends to move towards the inside of the bend and generate a secondary flow [53]. The low-momentum boundary layer migrates around the walls and rolls up to form a paired swirl pattern downstream of the bend. These secondary flows also interact with the shear layer of the flow separation at the inner bend, which is primarily driven by the adverse pressure gradient caused by the diffusing geometry [53]. The S-duct aerodynamics has been investigated with FRS and S-PIV measurements at the Aerodynamic Interface Plane (AIP), for an inlet centreline Mach number of 0.18, 0.27, and 0.40. However, for brevity, this analysis focuses on the operating point M_{ref} = 0.27, as the aerodynamics of S-duct intakes is insensitive to Mach number. Measured data at M_{ref} = 0.18 and 0.40 is included in the open access repository. These measurements highlight the expected S-duct flow topologies described above (Fig. 4). The distribution of the out-of-plane velocity component V_Z indicates the areas of low momentum and high momentum that are a product of the secondary flows and the first bend flow separation. The paired swirl pattern is highlighted by the in-plane velocity vectors, on the contour distribution of the out-of-plane velocity component V_Z.

FRS data shows good agreement with the S-PIV data in capturing the time-averaged distribution and magnitude of the 3-component velocity. It should be noted, that the FRS and S-PIV data have been acquired at a slightly different axial position (0.2 D_{in} for FRS and 0.0 D_{in} for S-PIV),
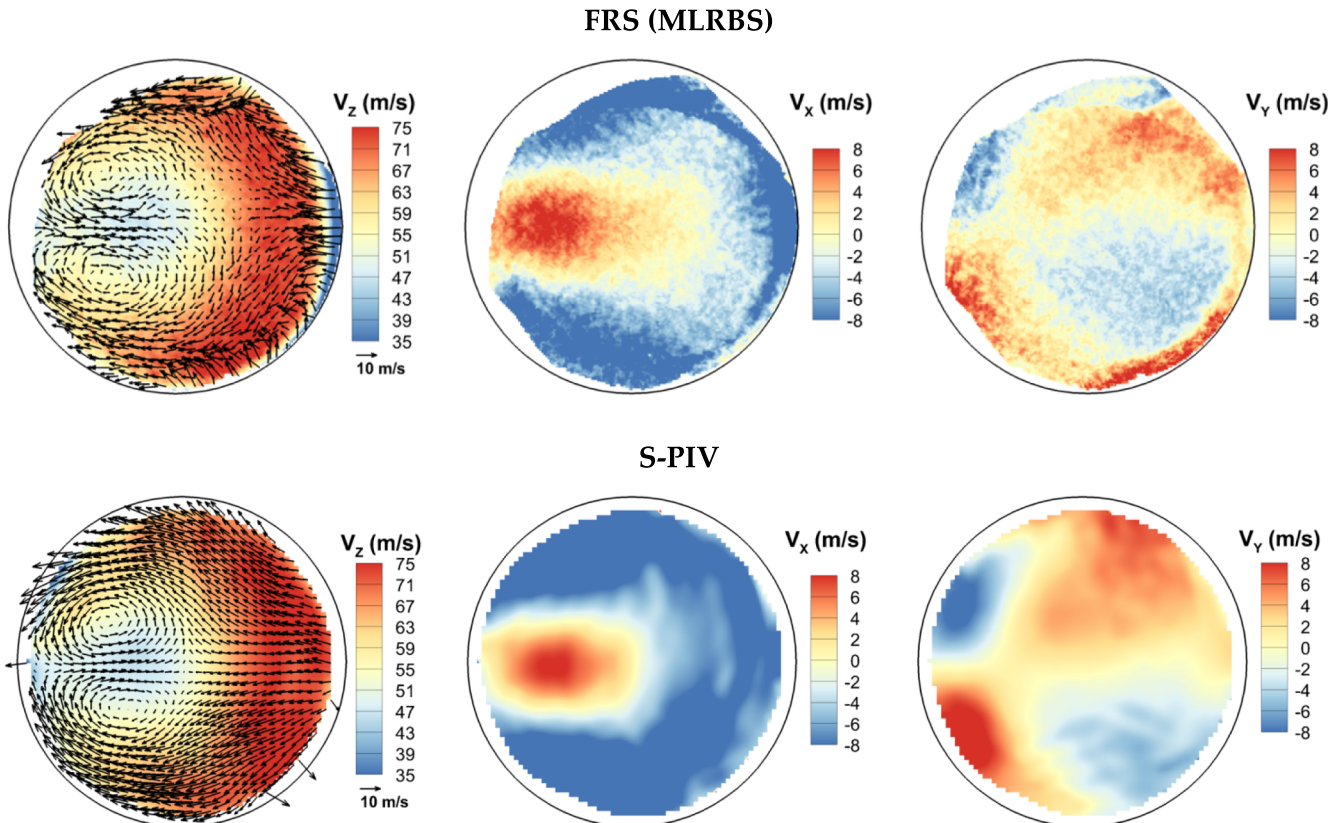

Fig. 4. Comparison of the velocity components measured with FRS evaluated with MLRBS methods and S-PIV at the S-duct outlet plane for inlet Mach = 0.27. In-plane velocity vectors on V_Z component are limited to a 4.5 mm spacing to improve clarity.

downstream of the S-duct outlet plane, due to the optical access constraints and arrangement. A slight discrepancy of results is therefore expected from flow mixing between the two planes. However, this only has a minor effect, as the relative distance of the planes was around 30 mm. Thus, to enable the comparison, the data presented in Fig. 5 has been self-normalized against the maximum value for both datasets. The RMSE of FRS data versus S-PIV measurements across the plane is approximately 3.3 % of the out-of-plane velocity component (V_Z). Some of this is attributed to the difference in spatial resolution that the two measurement methods offer, from the optical setup, processing methods and camera specification. The resulting spatial resolution of the FRS data was about 1.0 x 1.0 mm (Fig. 6), which is superior to the S-PIV data obtained with high-bandwidth cameras (2.3 x 2.3 mm). Nevertheless, it is envisaged that the resolution of FRS data would be comparable to modern low-speed sCMOS PIV cameras [54].

FRS presents several advances over S-PIV as it does not require seeding particles or high-quality optical access, which allows for the use of flexible fibre technology. These are turnkey considerations for flow diagnostics in embedded systems and in-flight environments, where an S-PIV requirement may not be possible [9]. In comparison with S-PIV, the FRS measurement allowed closer measurement to the AIP boundaries, as the bespoke flange [38] used to integrate the laser light-sheet at the AIP, drastically reduced the reflections of the laser in the optical domains (Fig. 2). For the S-PIV measurements, the laser light sheet illuminated a cross-flow plane in the transparent section of the intake (Fig. 1), which caused additional reflections at the boundaries and spurious vectors in the data processing thus limiting the data processing at $r/R_{AIP} < 0.9$. It is concluded that FRS is a candidate that is well positioned to offer solutions to measuring complex flows, with challenging optical access, and will likely introduce a step change in the measurement capability, once reaching higher technology readiness levels (TRL).

3.2. Rapid data processing with machine learning methods

The FRS data processing procedure is computationally heavy and time-consuming. For example, without the application of any machine learning methods, the computation of a single flow field from the data obtained from 6 views, each with 5 acquisition repetitions across 37 scanning frequencies with the current setup (Fig. 2), would take indicatively 440 CPU hours, on an average size processing machine with 4 2.8 Ghz cores. The introduction of machine learning methods to produce fast predictions of the Rayleigh-Brillouin Scattering (RBS) profile, MLRBS, reduced the computational time by 20 times [26] with negligible impact on the measurement accuracy. However, further improvements by a factor of 10 were seen with the application of machine learning to estimate the FRS intensity spectra directly, MLFRS [52] (Fig. 7). It is within the remit of the current work to report on the accuracy of MLFRS against the MLRBS approach.

A visual comparison of the flow fields including out-of-plane velocity, static pressure and temperature, and residuals from the fitting process of MLRBS and MLFRS is shown in Fig. 8 and Fig. 9. In S-duct diffusers, the static pressure topology is relatively uniform, with two areas of reduced static pressure, in correspondence of the twin-paired vortex structures [55]. The area-averaged isentropic static pressure, for an average Mach number of about $M = 0.2$ at the AIP, is expected to be about 5000 Pa below the reference ambient pressure (P_{ref}). However, these characteristics were not captured by the FRS measurements (Fig. 8). The overall flow field shows non-physical fluctuations of static pressure (P_S), that extend above the reference ambient pressure (P_{ref}). This is attributed to the effect of vibrations of the test section and the associated changes in the background conditions. The application of a normalization procedure and the fitting of background parameters caused a reduced pressure sensitivity and thus, FRS pressure results exhibit a lower quality, compared to 3C velocity measurements [38,44]. The static temperature field is expected to be relatively uniform across the plane, as heat sources are not introduced in the rig. The measured reduction of static pressure (T_S) relative to reference ambient conditions (T_{ref}) of approximately 3 K across the plane, is broadly aligned with the isentropic static temperature, for an average Mach number of about $M = 0.2$ at the AIP. However, erroneous measurements of static temperature are obtained in regions closer to the boundaries, likely caused by residual laser reflections and varying background conditions (Fig. 8). It is also acknowledged that the temperature fluctuations across the plane
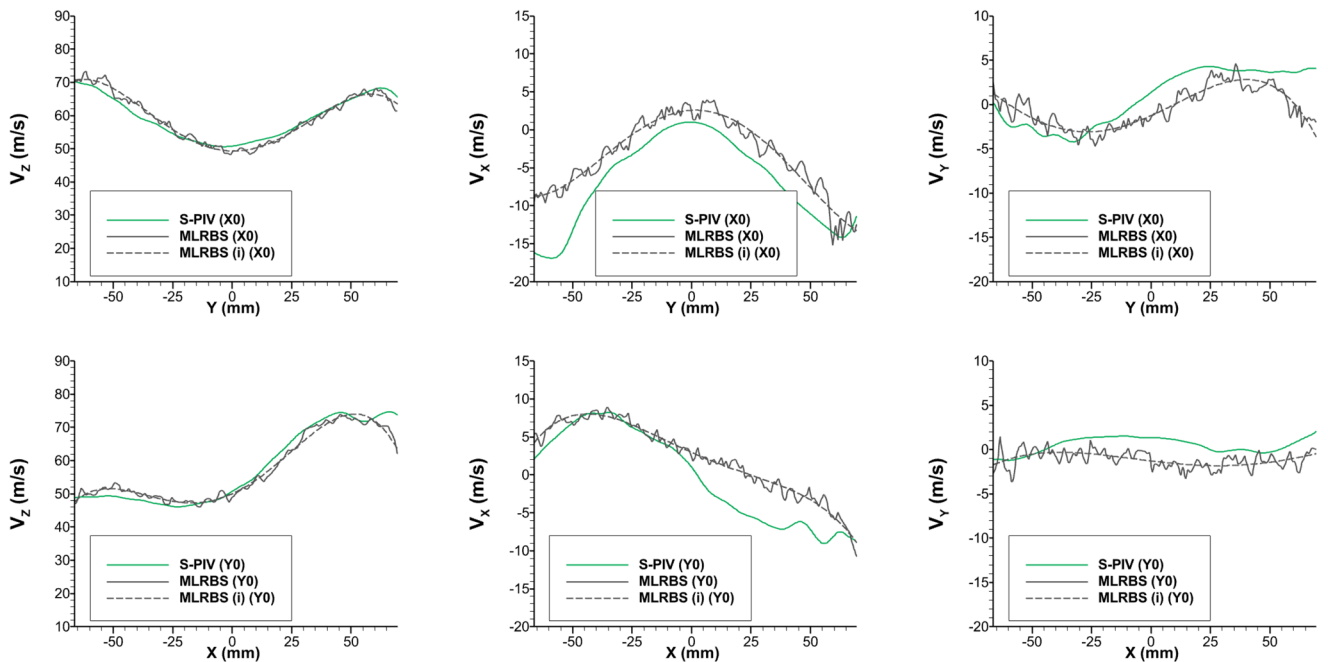

Fig. 5. Comparison of the velocity components derived with MLRBS methods on FRS data against S-PIV data along the horizontal (Y = 0) and vertical axis (X = 0) centred at the S-duct outlet plane for inlet Mach = 0.27. MLRBS (i) represents the FRS data interpolated on the PIV grid resolution for the RMSE evaluation against S-PIV data.
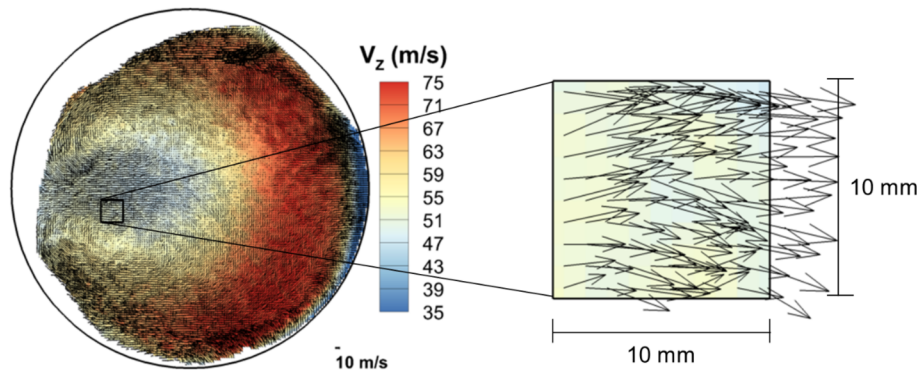
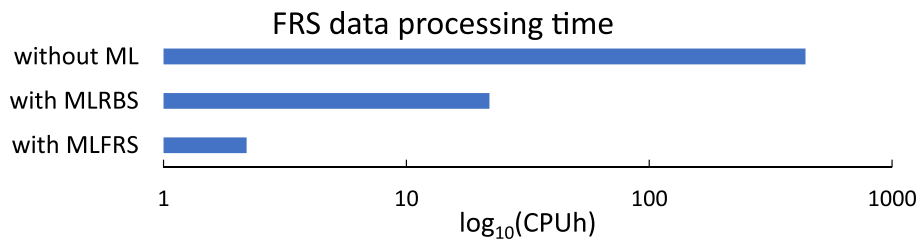**Fig. 6.** Vector distribution illustrating the resolution of the FRS measurements.

Fig. 7. Comparison of FRS data processing time between methods without machine learning, MLRBS, and MLFRS.
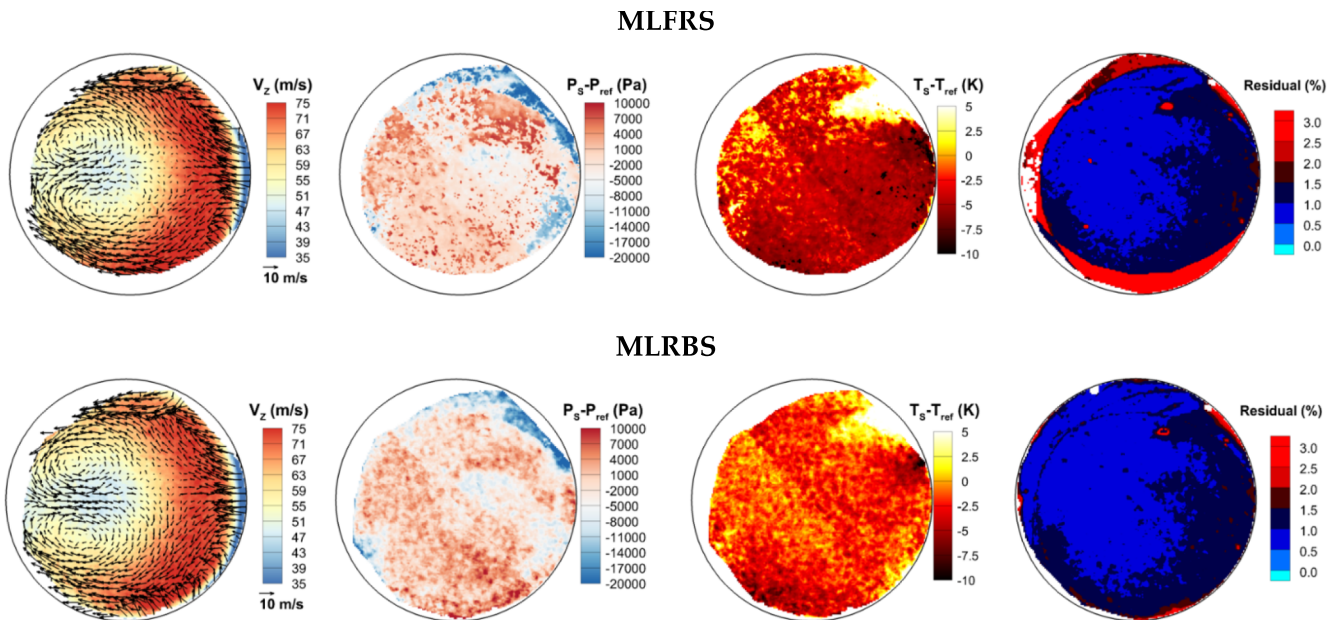

Fig. 8. Comparison of the flow fields derived with MLFRS and MLRBS methods at the S-duct outlet plane for inlet Mach = 0.27. In-plane velocity vectors on V_Z component are limited to a 4.5 mm spacing to improve clarity.

are due to the measurement uncertainty. In future work, it would be recommended to reduce the vibration at source, for example by de-coupling the support structures of the test rig from the mounting of laser optics.

Nevertheless, with acknowledged measurement errors for scalar components P_S and T_S, the data has been used for the comparison of MLFRS with MLRBS, as the methods are agnostic of the measurement conditions and configuration. The use of MLFRS to approximate the FRS intensity spectra proved successful, in the accurate reconstruction of the flow. The MLFRS has retained the key structure in the distribution of the velocity vectors, static pressure and temperature, compared to MLRBS

(Fig. 8). A step change in the residuals of the data fitting has been observed for MLFRS close to the boundaries (Fig. 8). The distribution of residuals correlates with the distribution of overlapping views from the 6 cameras (Fig. 3), in which areas that are seen by more cameras, have relatively lower fitting residuals, and vice versa. Thus multi-view setups, as the one proposed here, are especially suited for the exploitation of MLFRS methods, as they can lead to better approximations. Overall, the RMSE of MLFRS data versus MLRBS across the plane is approximately 0.91 % of the out-of-plane velocity component (V_Z) (Fig. 8). This is particularly relevant in relation to the 10-fold time savings in the vector and scalar computations, compared when adopting MLFRS instead of
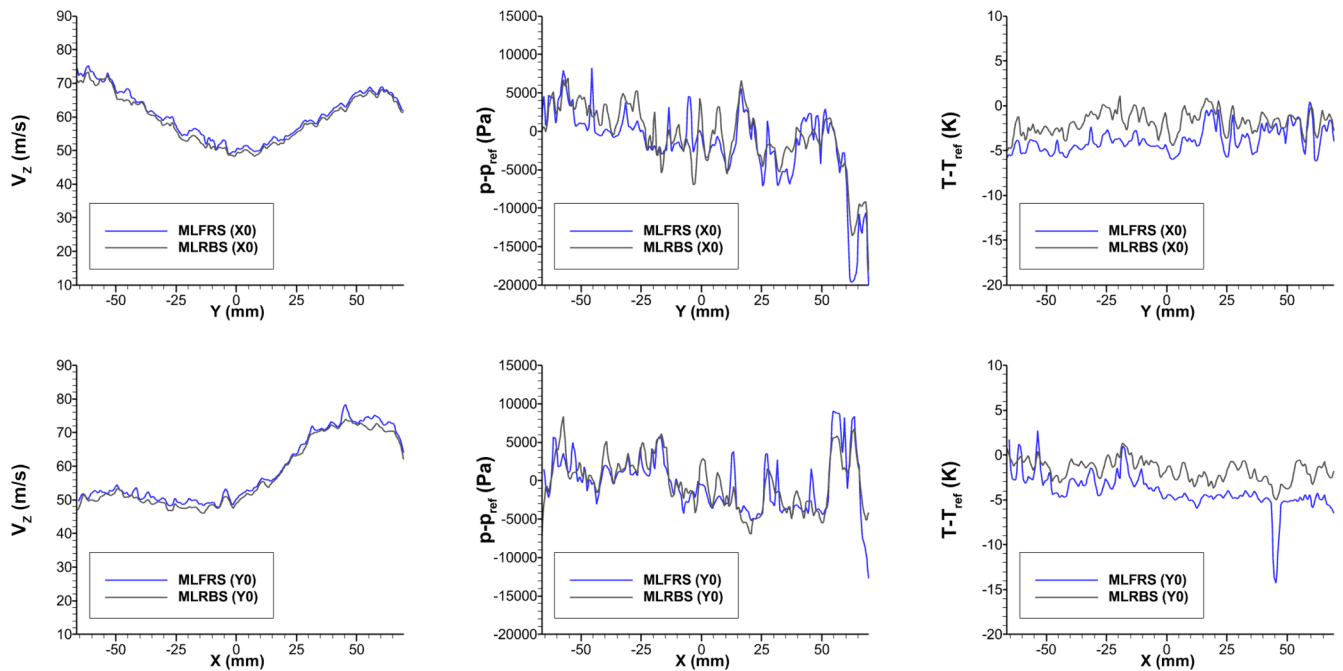
Fig. 9. Comparison of the velocity components derived with MLRBS and MLFRS methods along the horizontal (Y = 0) and vertical axis (X = 0) centered at the S-duct outlet plane for inlet Mach = 0.27.

MLRBS.

4. Conclusions

This work collates the recent advances in the development of a Filtered Rayleigh Scattering (FRS) measurement system for performing full-plane, intake distortion measurements with the potential for future in-flight applications. The research requirements led to the development of a novel FRS instrument, that employs a six-view observation concept, based on image fibre bundle technology, to simultaneously measure static pressure, temperature and 3D flow velocity fields. To benchmark the system's capability of capturing distorted intake flows, the FRS instrument was used to measure the aerothermal flow in a cross-sectional area, behind an S-duct diffuser. Complementary S-PIV measurements verified the quality of the FRS velocity results and matched the measurement within 90 % of the measured plane area, to within 3.3 % of RSME. This error is relatively low and comparable to typical uncertainty of S-PIV measurements, on the same configuration.

By introducing machine learning methods to the FRS data processing, a 200-fold increase in processing speed has been achieved with a 1 % penalty, on the accuracy of the out-of-plane velocity component. Although additional work is required to increase the technology readiness level of the system for industrial application, the measurement method can be considered superior to other non-intrusive methods, as the optical configuration is more flexible, where access is challenging. Furthermore, seeding particles are not required with FRS.

This work proposes a further development of the FRS technique for measuring inlet flow distortion in aero-engine intakes. The key novelties are the application of the FRS technique for intake flow distortion measurements in a laboratory-scale, convoluted diffuser geometry, the introduction MLFRS methods for rapid FRS processing and the relative quantification of the accuracy. The ability to assess multi-property flow distortion is also a key advantage, as it can contribute to understanding correlations between different distortion types, e.g. pressure and swirl. The experimental work leverages on the novel use of fibre optics for single-camera multi-view imaging systems, which can be integrated in future embedded or semi-embedded aero-engine intakes. As seeding is no longer required, this is expected to have a relevant impact on the measurement of in-flight test applications, in addition to the more traditional ground tests. The further implementation and development of machine learning, combined with availability of high-energy laser sources, can lead to real-time FRS data processing, that can be given as input to test engineers and, in the longer term, to the control system and pilot. This approach may be key to the reduction of risk for the operation of the propulsion system, throughout the flight mission.

CRediT authorship contribution statement

Matteo Migliorini: Writing – original draft, Visualization, Validation, Software, Resources, Project administration, Methodology, Investigation, Formal analysis, Data curation, Conceptualization. **Ulrich Doll:** Writing – review & editing, Writing – original draft, Visualization, Validation, Supervision, Software, Resources, Project administration, Methodology, Investigation, Funding acquisition, Formal analysis, Data curation, Conceptualization. **Nicholas J. Lawson:** Writing – review & editing, Writing – original draft, Supervision, Resources, Funding acquisition, Formal analysis, Conceptualization. **Sergey M. Melnikov:** Writing – original draft, Visualization, Validation, Software, Resources, Methodology, Investigation, Formal analysis, Data curation, Conceptualization. **Jonas Steinbock:** Writing – review & editing, Software, Resources, Methodology, Investigation. **Michael Dues:** Software, Resources, Project administration, Methodology, Investigation, Funding acquisition, Conceptualization. **Pavlos K. Zachos:** Writing – review & editing, Supervision, Project administration, Funding acquisition, Conceptualization. **Ingo Röhle:** Project administration, Funding acquisition. **David G. MacManus:** Writing – review & editing.

Declaration of competing interest

The authors declare that they have no known competing financial interests or personal relationships that could have appeared to influence the work reported in this paper.

Data availability

Data supporting this study are openly available from Cranfield University's repository CORD at DOI: 10.17862/cranfield.rd.25729647.

References

[1] ACARE, Flightpath 2050, Europe's Vision for Aviation, Publications Office of the European Union, Luxembourg, 2012. https://doi.org/10.2777/50266.
[2] Strategic Research & Innovation Agenda, ACARE, 2017. https://trimis.ec.europa.eu/sites/default/files/project/documents/acare-strategic-research-innovation-summary-2-interactive_0.pdf (accessed July 25, 2023).
[3] Strategic Implementation Plan, NASA, Washington D.C., US, 2019. https://www.nasa.gov/sites/default/files/atoms/files/sip-2019-v7-web.pdf (accessed July 25, 2023).
[4] J. Hoelzen, D. Silberhorn, T. Zill, B. Bensmann, R. Hanke-Rauschenbach, Hydrogen-powered aviation and its reliance on green hydrogen infrastructure – review and research gaps, Int. J. Hydrogen Energy 47 (2022) 3108–3130, https://doi.org/10.1016/j.ijhydene.2021.10.239.
[5] J. Bijewitz, A. Seitz, M. Hornung, B. Luftbarth, A review of recent aircraft concepts employing synergistic propulsion-airframe integration, in: 30th Congress of the International Council of the Aeronautical Sciences, Daejeon, Korea, 2016.
[6] E.J. Gunn, C.A. Hall, Aerodynamics of Boundary Layer Ingesting Fans, In: Proceedings of the ASME Turbo Expo 2014: Turbine Technical Conference and Exposition. Volume 1A: Aircraft Engine; Fans and Blowers, GT2014-26142, ASME, Düsseldorf, Germany, 2014. https://doi.org/10.1115/GT2014-26142.
[7] A. Castillo Pardo, C.A. Hall, Aerodynamics of boundary layer ingesting fuselage fans, J. Turbomach. 143 (2021), https://doi.org/10.1115/1.4049918.
[8] D.K. Hall, E.M. Greitzer, A. Uranga, M. Drela, S.A. Pandya, Inlet flow distortion in an advanced civil transport boundary layer ingesting engine installation, J. Turbomach. 144 (2022) 101002, https://doi.org/10.1115/1.4054035.
[9] Certification Specifications and Acceptable Means of Compliance for Engines (CS-E), European Aviation Safety Agency (EASA), 2020. https://www.easa.europa.eu/en/downloads/116287/en.
[10] F. Boden, N. Lawson, H.W. Jentink, J. Kompenhans, Advanced In-Flight Measurement Techniques, Springer Science & Business Media, 2013.
[11] Anatomy of a solution: how our testbed helps advancements take flight, Rolls Royce. https://www.rolls-royce.com/media/our-stories/discover/2019/trent1000-updates-10-01-19.aspx (accessed July 25, 2023).
[12] Honeywell Flying Lab Relies On 'Golden Engine,' Honeywell Aerospace. https://aerospace.honeywell.com/us/en/about-us/blogs/honeywell-flying-lab-relies-on-golden-engine (accessed July 25, 2023).
[13] Design and development of an F/A-18 inlet distortion rake - A cost and time saving solution, in: Biennial Flight Test Conference, American Institute of Aeronautics and Astronautics, Hilton Head,SC,U.S.A., 1994. https://doi.org/10.2514/6.1994-2132.
[14] C. Dunker, An in-flight investigation of a turbulent boundary layer at Reynolds numbers up to Re_theta = 49,400, Exp. Fluids 62 (2020) 4, https://doi.org/10.1007/s00348-020-03072-9.
[15] C. Dunker, R. Geisler, Full-Scale In-Flight Flow Investigation of a High-Lift Vortex System by Means of Particle Image Velocimetry, in: A. Dillmann, G. Heller, E. Krämer, C. Wagner, S. Bansmer, R. Radespiel, R. Semaan (Eds.), New Results in Numerical and Experimental Fluid Mechanics XI, Springer International Publishing, Cham, 2018, pp. 523–532, https://doi.org/10.1007/978-3-319-64519-3_47.
[16] C. Tropea, A.L. Yarin, J.F. Foss (Eds.), Springer Handbook of Experimental Fluid Mechanics, Springer, Berlin, Heidelberg, 2007, https://doi.org/10.1007/978-3-540-30299-5.
[17] M. Raffel, C.E. Willert, S.T. Wereley, J. Kompenhans, S. Willert, S.T. Wereley, J. Kompenhans, Particle Image Velocimetry: A Practical Guide, in: Springer-VerlagSpringer-Verlag (Ed.), Particle Image Velocimetry, Springer, Berlin, 2007, pp. 203–241.
[18] H. Komine, System for measuring velocity field of fluid flow utilizing a laser-doppler spectral image converter, US4919536A, 1990. https://patents.google.com/patent/US4919536/en (accessed July 27, 2023).
[19] T. Guimarães, K.T. Lowe, W.F. O'Brien, StreamVane turbofan inlet swirl distortion generator: mean flow and turbulence structure, J. Propul. Power 34 (2017) 340–353, https://doi.org/10.2514/1.B36422.
[20] P.K. Zachos, D.G. MacManus, D.G. Prieto, N. Chiereghin, Flow distortion measurements in convoluted aeroengine intakes, AIAA J. 54 (2016) 2819–2832, https://doi.org/10.2514/1.J054904.
[21] D. Gil-Prieto, P.K. Zachos, D.G. MacManus, G. McLelland, Unsteady characteristics of S-duct intake flow distortion, Aerosp. Sci. Technol. 84 (2019) 938–952, https://doi.org/10.1016/j.ast.2018.10.020.
[22] M. Migliorini, P.K. Zachos, D.G. MacManus, Novel method for evaluating intake unsteady flow distortion, J. Propul. Power (2021) 1–13, https://doi.org/10.2514/1.B38127.
[23] M. Migliorini, P.K. Zachos, D.G. MacManus, P. Haladuda, S-duct flow distortion with non-uniform inlet conditions, Proceed. Inst. Mech. Eng., Part G: J. Aerospace Eng. (2022) 095441002211016, https://doi.org/10.1177/09544100221101669.
[24] G. McLelland, D.G. MacManus, P.K. Zachos, D. Gil-Prieto, M. Migliorini, Influence of upstream total pressure profiles on S-duct intake flow distortion, J. Propul. Power 36 (2020) 346–356, https://doi.org/10.2514/1.B37554.
[25] I. Röhle, Laser Doppler Velocimetry auf der Basis frequenzselektierter Absorption: Aufbau und Einsatz eines Doppler Global Velocimeters, Ph. D. Dissertation, DLR-Forschungsbericht, 1999. https://elib.dlr.de/996/.
[26] U. Doll, M. Migliorini, J. Baikie, P.K. Zachos, I. Röhle, S. Melnikov, J. Steinbock, M. Dues, R. Kapulla, D.G. MacManus, N.J. Lawson, Non-intrusive flow diagnostics for unsteady inlet flow distortion measurements in novel aircraft architectures, Prog. Aerosp. Sci. 130 (2022) 100810, https://doi.org/10.1016/j.paerosci.2022.100810.
[27] S.W. Powers, G. Byun, K.T. Lowe, Validation of filtered rayleigh scattering optical rake measurement techniques in turbomachinery applications and boundary layers, J. Turbomach. 146 (2023), https://doi.org/10.1115/1.4063562.
[28] K.T. Lowe, Laser velocimetry for turbofan inlet distortion applications, Aircr. Eng. Aerosp. Technol. 92 (2019) 20–26, https://doi.org/10.1108/AEAT-11-2018-0285.
[29] U. Doll, G. Stockhausen, C. Willert, Pressure, temperature, and three-component velocity fields by filtered Rayleigh scattering velocimetry, Opt. Lett. 42 (2017) 3773–3776, https://doi.org/10.1364/OL.42.003773.
[30] U. Doll, I. Röhle, M. Dues, R. Kapulla, Time-resolved multi-parameter flow diagnostics by filtered Rayleigh scattering: system design through multi-objective optimisation, Meas. Sci. Technol. 33 (2022) 105204, https://doi.org/10.1088/1361-6501/ac7cca.
[31] U. Doll, R. Kapulla, M. Dues, J. Steinbock, S. Melnikov, I. Röhle, M. Migliorini, P.K. Zachos, Towards time-resolved multi-property measurements by filtered Rayleigh scattering: diagnostic approach and verification, Exp. Fluids 65 (2024), https://doi.org/10.1007/s00348-023-03740-6.
[32] A.K.M.F. Hussain, V. Ramjee, Effects of the axisymmetric contraction shape on incompressible turbulent flow, J. Fluids Eng. 98 (1976) 58–68, https://doi.org/10.1115/1.3448210.
[33] G. Tanguy, D.G. MacManus, E. Garnier, P.G. Martin, Characteristics of unsteady total pressure distortion for a complex aero-engine intake duct, Aerosp. Sci. Technol. 78 (2018) 297–311, https://doi.org/10.1016/j.ast.2018.04.031.
[34] D. Gil-Prieto, D.G. MacManus, P.K. Zachos, G. Tanguy, K.R. Menzies, Convoluted intake distortion measurements using stereo particle image velocimetry, AIAA J. 55 (2017) 1878–1892, https://doi.org/10.2514/1.J055467.
[35] D.G. MacManus, N. Chiereghin, D.G. Prieto, P. Zachos, Complex aeroengine intake ducts and dynamic distortion, AIAA J. 55 (2017) 2395–2409, https://doi.org/10.2514/1.J054905.
[36] G. Tanguy, D.G. MacManus, P. Zachos, D. Gil-Prieto, E. Garnier, Passive flow control study in an S-duct using stereo particle image velocimetry, AIAA J. 55 (2017) 1862–1877, https://doi.org/10.2514/1.J055354.
[37] E. Garnier, Flow control by pulsed jet in a curved S-Duct: a spectral analysis, AIAA J. 53 (2015) 2813–2827, https://doi.org/10.2514/1.J053422.
[38] M. Migliorini, P.K. Zachos, D.G. MacManus, U. Doll, M. Dues, S.J. Jonas, F. Dues, A. Siswanto, S.M. Melnikov, I. Rohle, Seeding-free inlet flow distortion measurements using filtered Rayleigh scattering: integration in a complex intake test facility, in: AIAA Sci-Tech Forum, 2024, p. 2831, https://doi.org/10.2514/6.2024-2831.
[39] R. Miles, W. Lempert, Two-dimensional measurement of density, velocity, and temperature in turbulent high-speed air flows by UV Rayleigh scattering, Appl. Phys. B 51 (1990) 1–7, https://doi.org/10.1007/BF00332317.
[40] J.N. Forkey, N.D. Finkelstein, W.R. Lempert, R.B. Miles, Demonstration and characterization of filtered Rayleigh scattering for planar velocity measurements, AIAA J. 34 (1996) 442–448, https://doi.org/10.2514/3.13087.
[41] M. Boguszko, G.S. Elliott, On the use of filtered Rayleigh scattering for measurements in compressible flows and thermal fields, Exp. Fluids 38 (2005) 33–49, https://doi.org/10.1007/s00348-004-0881-4.
[42] U. Doll, G. Stockhausen, C. Willert, Endoscopic filtered Rayleigh scattering for the analysis of ducted gas flows, Exp. Fluids 55 (2014) 1690, https://doi.org/10.1007/s00348-014-1690-z.
[43] G. Bradski, The OpenCV Library, Dr. Dobb's J. Soft. Tools 120 (2000) 122–125.
[44] U. Doll, E. Burow, G. Stockhausen, C. Willert, Methods to improve pressure, temperature and velocity accuracies of filtered Rayleigh scattering measurements in gaseous flows, Measure. Sci. Tech. 27 (12) (2016), https://doi.org/10.1088/0957-0233/27/12/125204.
[45] G.J. Hunt, C.R. Ground, R.L. Hunt, Fast approximations of spectral lineshapes to enable optimization of a filtered Rayleigh scattering experiment, Meas. Sci. Technol. 31 (2020) 095203, https://doi.org/10.1088/1361-6501/ab8a7e.
[46] B. Witschas, Analytical model for Rayleigh-Brillouin line shapes in air, Appl. Opt. 50 (2011) 267–270, https://doi.org/10.1364/AO.50.000267.
[47] Y. Ma, F. Fan, K. Liang, H. Li, Y. Yu, B. Zhou, An analytical model for Rayleigh-Brillouin scattering spectra in gases, J. Opt. 14 (9) (2012), https://doi.org/10.1088/2040-8978/14/9/095703.
[48] I. Binietoglou, P. Giampouras, L. Belegante, Linear approximation of Rayleigh-Brillouin scattering spectra, Appl. Opt. 55 (2016) 7707, https://doi.org/10.1364/AO.55.007707.
[49] G. Tenti, C.D. Boley, R.C. Desai, On the kinetic model description of Rayleigh-Brillouin Scattering from molecular gases, Can. J. Phys. (2011), https://doi.org/10.1139/p74-041.
[50] X. Pan, M.N. Shneider, R.B. Miles, Coherent Rayleigh-Brillouin scattering in molecular gases, Phys. Rev. A 69 (2004) 033814, https://doi.org/10.1103/PhysRevA.69.033814.

[51] F. Pedregosa, G. Varoquaux, A. Gramfort, V. Michel, B. Thirion, O. Grisel, M. Blondel, P. Prettenhofer, R. Weiss, V. Dubourg, J. Vanderplas, A. Passos, D. Cournapeau, M. Brucher, M. Perrot, É. Duchesnay, Scikit-learn: machine learning in python, J. Mach. Learn. Res. 12 (2011) 2825–2830.

[52] S.M. Melnikov, I. Röhle, U. Doll, M. Dues, J. Steinbock, M. Migliorini, P.K. Zachos, Machine learning approach for fast evaluation of filtered Rayleigh scattering measurement data, in: Deutschen Gesellschaft für Laser-Anemometrie GALA e.V., München, Deutschland, 2023. https://gala-ev.org/images/Beitraege/Beitraege2023/pdf/03.pdf.

[53] E.M. Greitzer, C.S. Tan, M.B. Graf, Generation of streamwise vorticity and three-dimensional flow, in: Internal Flow, Cambridge University Press, 2004, pp. 446–505, https://doi.org/10.1017/CBO9780511616709.011.

[54] K.U. Kempaiah, T. Piovesan, P.K. Zachos, D. Michaelis, R. Gebbink, B. Van Rooijen, D.G. Prieto, D. MacManus, A. Sciacchitano, C. Sheaf, High-resolution turbofan intake flow characterization by automated stereoscopic-PIV in an industrial wind tunnel environment, Meas. Sci. Technol. 35 (2024) 025210, https://doi.org/10.1088/1361-6501/ad0ea0.

[55] S.R. Wellborn, B.A. Reichert, T.H. Okiishi, "An experimental investigation of the flow in a diffusing S-duct," AIAA 1992-3622. *28th Joint Propulsion Conference and Exhibit*. July 1992.

Advancements on the use of Filtered Rayleigh Scattering (FRS) with machine learning methods for flow distortion in aero-engine intakes

Migliorini, Matteo